Water Splitting Very Important Paper

How to cite: *Angew. Chem. Int. Ed.* **2021**, *60*, 8243–8250
International Edition: doi.org/10.1002/anie.202016199
German Edition: doi.org/10.1002/ange.202016199

Exclusive Strain Effect Boosts Overall Water Splitting in PdCu/Ir Core/Shell Nanocrystals

Menggang Li[+], Zhonglong Zhao[+], Zhonghong Xia, Mingchuan Luo, Qinghua Zhang, Yingnan Qin, Lu Tao, Kun Yin, Yuguang Chao, Lin Gu, Weiwei Yang, Yongsheng Yu, Gang Lu, and Shaojun Guo**

Abstract: *Core/shell nanocatalysts are a class of promising materials, which achieve the enhanced catalytic activities through the synergy between ligand effect and strain effect. However, it has been challenging to disentangle the contributions from the two effects, which hinders the rational design of superior core/shell nanocatalysts. Herein, we report precise synthesis of PdCu/Ir core/shell nanocrystals, which can significantly boost oxygen evolution reaction (OER) via the exclusive strain effect. The heteroepitaxial coating of four Ir atomic layers onto PdCu nanoparticle gives a relatively thick Ir shell eliminating the ligand effect, but creates a compressive strain of ca. 3.60%. The strained PdCu/Ir catalysts can deliver a low OER overpotential and a high mass activity. Density functional theory (DFT) calculations reveal that the compressive strain in Ir shell downshifts the d-band center and weakens the binding of the intermediates, causing the enhanced OER activity. The compressive strain also boosts hydrogen evolution reaction (HER) activity and the strained nanocrystals can be served as excellent catalysts for both anode and cathode in overall water-splitting electrocatalysis.*

Introduction

Increasingly hydrogen-related energy devices, including hydrogen-oxygen fuel cells, large-scale hydrogen power generation and other hydrogen-powered devices, etc. have stimulated the development of various hydrogen evolution technologies.[1–3] In particular, the electrochemical overall water splitting, representing one of the most eco-friendly and high-efficient techniques for hydrogen production, has been deemed to be an up-and-coming trend to realize such sustainable energy scheme.[3–6] Since the activities of electrocatalysts toward oxygen and hydrogen evolution reaction (OER and HER) determine the efficiency of electrocatalytic overall water splitting, the rational design of high-performance electrocatalysts appears to be particularly significant.[7–9] In terms of activity and stability, especially in the acidic environment, noble metals-based catalysts are still irreplaceable.[10–13] In addition, compared to the cathodic HER process, the four-electron OER process at the anode is considerably more sluggish, dominating the total potential of the overall water electrolyzers.[14–16]

To boost OER and HER reactions, Ir-based core/shell nanocatalysts have been developed, which exhibit increased activities.[14,17–20] However, the underlying mechanism of the increasement remains murky. This is largely due to the fact that two intertwined mechanisms, i.e., ligand effect and strain effect, are at play in these core/shell nanocatalysts.[19,21–23] And it has been exceedingly difficult to disentangle the respective contributions, which is particularly troublesome when the two effects have opposite contributions.[21,24] Indeed, not knowing the relative importance of the two effects has significantly hampered the development of superior core/shell nanocatalysts.

In this work, we overcome the challenge by tailoring the shell thickness of PdCu/Ir core/shell nanocrystals. Our research is motivated by the observation that the ligand effect disappears beyond 3 atomic layers whereas the strain effect remains effective at 5 atomic layers.[21,24,25] This crucial difference reflects the fact that the ligand effect originates

[*] M. Li,[+] Z. Xia, M. Luo, Y. Qin, L. Tao, K. Yin, Y. Chao, Prof. S. Guo
School of Materials Science and Engineering, Peking University
Beijing 100871 (China)
E-mail: guosj@pku.edu.cn

M. Li,[+] Prof. W. Yang, Prof. Y. Yu
MIIT Key Laboratory of Critical Materials Technology for New Energy Conversion and Storage, School of Chemistry and Chemical Engineering, Harbin Institute of Technology
Harbin, Heilongjiang 150001 (China)

Z. Zhao[+]
School of Physical Science and Technology, Inner Mongolia University
Hohhot 010021 (China)

Prof. G. Lu
Department of Physics and Astronomy, California State University Northridge
Northridge, CA 91330 (USA)
E-mail: ganglu@csun.edu

Q. Zhang, Prof. L. Gu
Beijing National Laboratory for Condensed Matter Physics, Institute of Physics, Chinese Academy of Sciences
Beijing 100190 (China)

Prof. S. Guo
BIC-ESAT, College of Engineering, Peking University
Beijing 100871 (China)

[+] These authors contributed equally to this work.

Supporting information and the ORCID identification number(s) for the author(s) of this article can be found under: https://doi.org/10.1002/anie.202016199.

from the charge transfer between the core/shell materials, while the strain effect arises from the lattice mismatch between them.[24,26,27] Therefore, if one could develop a core/shell nanocatalyst with a shell thickness of ≈4 atomic layers, one can essentially eliminate the contribution of the ligand effect and achieve a core/shell system with the exclusive strain effect. The separation of the two effects enables us to derive a clear picture on how strain could modulate the activity of the core/shell nanocatalysts. This picture when combined with future study on thinner shells may help us gain better understanding of the ligand effect as well. Thus, the novel PdCu/Ir nanocatalyst with 4 layers of Ir represents an ideal system to elucidate the underlying mechanism of enhanced electrocatalytic activities.

In the following, we report the precise tuning of heteroepitaxial coating of ≈4 monolayer (ML) Ir shells onto the PdCu nanocrystals to get the exclusive strained PdCu/Ir core/shell nanocrystals. The lattice strain is induced by the epitaxial growth of lattice-mismatched Ir shell, achieving a compressive strain of 3.60% for Ir, which considerably modulates the adsorption abilities of rate-determining intermediates. As a result, the strained PdCu/Ir core/shell nanocrystals exhibit a low OER overpotential of 283 mV at a current density of 10 mA cm^{-2} and a high mass activity of 1.83 A mg_{Ir}^{-1} at 1.51 V (vs. RHE) in acidic media, much better than the unstrained multi-metallic alloyed counterparts. Density functional theory (DFT) calculations further confirm the dominating role of compressive strain in OER performance enhancements by presenting the influence of heteroepitaxial lattice strain on the adsorption strength toward oxygenated intermediates. Finally, the strained PdCu/Ir core/shell nanocrystals also show a low overpotential of 20 mV toward HER, thus realizing a high active and stable electrocatalytic overall water splitting electrolyzer with a cell voltage of 1.583 V at 10 mA cm^{-2}.

Results and Discussion

The PdCu/Ir core/shell nanocrystals were synthesized via a controlled deposition of 4 ML Ir shell on the pre-synthesized PdCu nanocrystals (Figure S1). As-obtained PdCu/Ir core/shell nanocrystals are monodisperse with a size of ≈9.5 nm, determined by the transmission electron microscopy (TEM) and high-angle annular dark-field scanning TEM (HAADF-STEM) images (Figure 1 a,b & S2). The power X-ray diffraction (PXRD) pattern of PdCu/Ir nanocrystals exhibits a typical face-centered cubic (*fcc*) structure, where several diffraction peaks are located between those of *fcc* Pd (JCPDS No. 46-1043) and *fcc* Cu (JCPDS No. 04-0836) (Figure 1 c), and no additional diffraction peaks of Ir can be observed. The atomic ratio of Pd/Cu/Ir in PdCu/Ir nanocrystals is 26/65/9, determined by the STEM energy-dispersive X-ray spectroscopy (STEM-EDS), which is in line with the results of inductively coupled plasma-atomic emission spectroscopy (ICP-AES) (Figure 1 d). The high crystallinity can be revealed by the high-resolution TEM (HRTEM) image taken from individual PdCu/Ir nanocrystal (Figure 1 e). The well-resolved lattice spacing is 0.216 nm, in accordance with the (111) plane of *fcc* PdCu. The corresponding fast

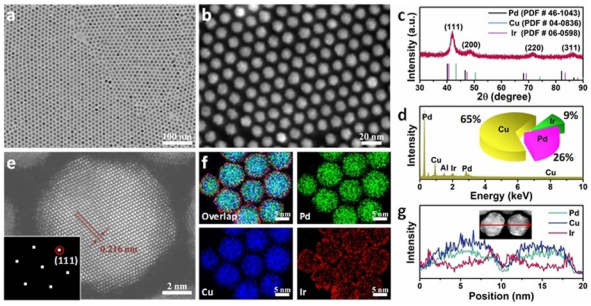

Figure 1. Structural and compositional characterization of PdCu/Ir core/shell nanocrystals. Representative a) low-magnification and b) HAADF-STEM images, c) PXRD pattern, d) STEM-EDS spectra (inset is the corresponding ICP-AES result), e) atomic-resolution HAADF-STEM image (inset is the corresponding FFT pattern), f) elemental EDS mapping and g) line-scanning profiles across the red arrow shown in the inset of the image of PdCu/Ir nanocrystals.

Fourier transform (FFT) pattern further confirms the high crystallinity and the presence of (111) plane of *fcc* PdCu (the *inset* of Figure 1 e). The EDS mapping under HAADF-STEM mode shows that the Ir species are surface segregation, while Pd and Cu species uniformly distribute throughout the whole core of nanocrystal, providing direct evidence for the formation of core/shell structure (Figure 1 f). The EDS line scan image exhibits good matching with Ir trace located at the edges while Pd and Cu traces concentrated at the center (Figure 1 g). The thickness of surface Ir shell is estimated to be 0.8 nm, corresponding to about 4 atomic layers. According to the Vegard law, the lattice constant of $Pd_{26}Cu_{65}$ core can be calculated to be 2.14 Å, while that of Ir shell is 2.22 Å. The interfacial lattice mismatch between the PdCu core and Ir shell induces the accommodated compressive strain of 3.60%, determined by the following equation: $s(\mathrm{Ir}) = (\alpha_{\mathrm{Ir}} - \alpha_{\mathrm{shell}})/\alpha_{\mathrm{shell}}$, where α_{Ir} and α_{shell} represent the lattice constant of Ir shell and PdCu core, respectively.[25,26,28] In contract, unlike the PdCu/Ir core/shell nanocrystals where Ir atoms are segregated on the surface, the trimetallic PdCuIr alloys with perfect *fcc* crystalline structure possess a random occupation of Pd, Cu and Ir, which significantly minimizes the strain. Such compressive lattice-strain makes the strained PdCu/Ir core/shell nanocrystals possible to boost the electrocatalytic performance.

The PdCu and PdCuIr bi/trimetallic nanocrystals with the morphology, composition and sizes similar to PdCu/Ir can also be synthesized via a modified synthesis method (Figure S3). STEM-EDS spectra and ICP-AES results collectively reveal that the ratio of Pd/Cu in PdCu bimetallic nanocrystals and that of Pd/Cu/Ir in PdCuIr trimetallic nanocrystals are 25/75 and 26/65/9, respectively (Figure S4). PXRD patterns reveal the typical *fcc* structures of alloyed PdCu and PdCuIr nanocrystals (Figure S5). The catalysts used for electrochemical tests were prepared by quantitatively depositing three nanocrystals (PdCu, PdCuIr and PdCu/Ir) onto the commercial carbon supports (Ketjen Black-300J), and subsequently thermal annealing to remove excess surfactants around the surface of catalysts (Figure S6). The resulting well-dispersed carbon supported nanocrystal

catalysts are denoted as PdCu/C, PdCuIr/C and PdCu/Ir/C, respectively.

We first investigated the OER activities of three catalysts and commercial Ir/C under 0.1 M $HClO_4$ electrolyte. The OER polarization curves were conducted in O_2-saturated 0.1 M $HClO_4$ electrolyte at 5 mV s^{-1} (Figure 2a). Among several measured catalysts, the PdCu/Ir/C shows the lowest onset potential of 1.44 V (vs. RHE) with the order of PdCu/Ir/C < PdCuIr/C ≈ Ir/C < PdCu/C. In addition, the Tafel slopes are further derived to reveal the OER reaction kinetics (Figure 2b). Specifically, the calculated Tafel slopes of PdCu/Ir/C, PdCuIr/C, PdCu/C and Ir/C are 59.6, 77.1, 210.8 and 62.6 mV dec^{-1}, respectively (Figure 2c). This confirms that the strained PdCu/Ir core/shell structure can exhibit higher reaction rate and faster kinetics toward water oxidation. To afford a current density of 10 mA cm^{-2}, the PdCu/Ir/C only requires the overpotential of 283 mV, 55 and 65 mV lower than those of Ir/C and PdCuIr/C, respectively (Figure 2c). In light of the noble metals, such as Ir and Pd, are applied for this catalytic system, we normalized the mass activities at 1.51 V (vs. RHE) based on the real mass of noble metal determined by ICP-AES (Figure 2d). The PdCu/Ir/C exhibits a high mass activity of 1.19 A mg_{Pd+Ir}^{-1}, almost 18.5, 7.1 and 6.5 folds higher than those of PdCu/C (0.06 A mg_{Pd}^{-1}), PdCuIr/C (0.16 A mg_{Pd+Ir}^{-1}) and Ir/C (0.18 A mg_{Ir}^{-1}), respectively, indicating the ultrahigh noble metal utilization of PdCu/Ir/C. More surprisingly, due to the low content of Ir atoms, the PdCu/Ir/C possesses the highest Ir atomic utilization among these Ir-contained catalysts (the *inset* of Figure 2d). The PdCu/Ir/C exhibits the highest OER mass activity of 1.83 A mg_{Ir}^{-1} at 1.51 V (vs. RHE), while those of the PdCuIr/C and Ir/C are only 0.41 A mg_{Ir}^{-1} and 0.18 A mg_{Ir}^{-1}, respectively. The normalized mass activities at 1.50 V (vs. RHE) further reveal the enhanced OER activity of the strained core/shell structure (Figure S7). The current overpotential and mass activity of PdCu/Ir/C represent one of the best level of the Ir-based OER electrocatalysts in acidic conditions *yet* reported (Figure 2e & Table S1).[29–38]

Stability, as one of the most important issues of electrocatalysts, is also evaluated by accelerated durability tests (ADTs) and chronoamperometry (CP) measurement. After 2000 CV cycles between 1.40 and 1.65 V (vs. RHE) before IR correction at an accelerated scan rate of 50 mV s^{-1}, the overpotential of PdCu/Ir/C at a current density of 10 mA cm^{-2} only increases 5 mV (Figure 2f). Furthermore, there is almost no change during 15 h electrocatalytic process at 10 mA cm^{-2} in the CP curve, further confirming the long-term stability of PdCu/Ir/C (the *inset* of Figure 2f). In addition, the PdCu/Ir/C shows almost on morphological change and a little variation of composition from 26/65/9 to 23/46/31 (Figure S8) after long-term durability tests. These result reveal that as-synthesized PdCu/Ir/C catalysts are highly stable for OER electro-

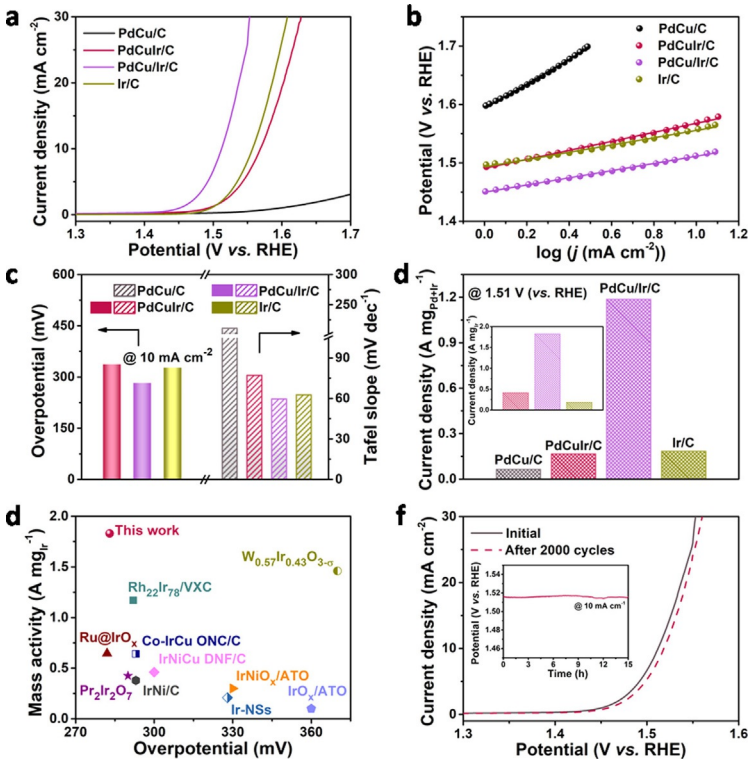

Figure 2. The electrocatalytic OER performance of different electrocatalysts in 0.1 M $HClO_4$. a) The OER polarization curves, b) the corresponding Tafel slope plots, c) the overpotential at a current density of 10 mA cm^{-2} (left) and the corresponding Tafel slopes (right), and d) current density normalized by the noble metal mass (inset is current density normalized by the Ir mass) at 1.51 V (vs. RHE) of different electrocatalysts. e) Comparison of the OER catalytic performance of the PdCu/Ir/C electrocatalyst with those of other representative Ir-based OER electrocatalysts reported recently in acidic media.[29–28] f) OER polarization curves before and after 2000 cycles (inset is CP measurement at 10 mA cm^{-2}) of PdCu/Ir/C.

catalysis, which is probably caused by their unique core/shell structure.

As far as the core/shell structures with a shell atomic layer ≥ 4 ML are concerned, strain effect becomes a dominated factor for enhanced electrocatalytic activity.[25,39] Generally, a desired catalyst should have an optimized adsorption strength for the catalytic reaction intermediates, which is neither too strong nor too weak.[39–41] With respect to OER, the complex process unfavorable for reaction kinetics involves four proton-coupled electron transfers and O–O bond formation, which can be optimized by the compressive strain.[13,42] The compressive strain is facilitated to the adsorption of oxygen-containing intermediates (HO*, O* and HOO*, etc.), therefore making the production of molecular oxygen much easier. In order to deeply understand the variation of electronic structure between PdCu/Ir core/shell and alloyed PdCuIr nanocrystals, high-resolution X-ray photoelectron spectroscopy (XPS) were further carried out and deconvoluted. Figure 3 a,b & S9 show the Pd 3d, Ir 4f and Cu 2p spectra of PdCu/Ir and PdCuIr nanocrystals, respectively. The Pd 3d spectra can be divided into two peaks corresponding to the Pd $3d_{5/2}$ and Pd $3d_{3/2}$ states, and be further split into two double peaks assigned to the Pd^0 and Pd^{2+} chemical states. Similarly, the Cu 2p and Ir 4f spectra also show two pairs of doublets, associated with Cu^0 $2p_{3/2}$, Cu^0 $2p_{1/2}$, Cu^{2+} $2p_{3/2}$, Cu^{2+} $2p_{1/2}$ and Ir^0 $4f_{7/2}$, Ir^0 $4f_{5/2}$, Ir^{4+} $4f_{7/2}$, Ir^{4+} $4f_{5/2}$, respectively. All the metal atoms in both PdCuIr and PdCu/Ir nanocrystals are mainly in the metallic state. Noted that both Pd 3d and Cu 2p spectra of PdCu/Ir are negatively shifted to higher binding energies compared with those of PdCuIr alloys, while the Ir 4f spectra are blueshifted positively. Such strongly peak shift visualizes a strong change in the surface electronic structure of PdCu/Ir nanocrystals, originated from inter-atomic or intra-atomic charge transfer from Ir to Pd or Cu, which leads to a weak adsorption for reaction intermediates on the surface of PdCu/Ir nanocrystals.[43–45] The modified adsorption/desorption energy of reaction intermediate is in line with d-band center downward relative to the Fermi level, thus affecting the electrocatalytic activity.[45,46]

DFT calculations were further performed to provide insights into the origin of the enhanced OER performance on

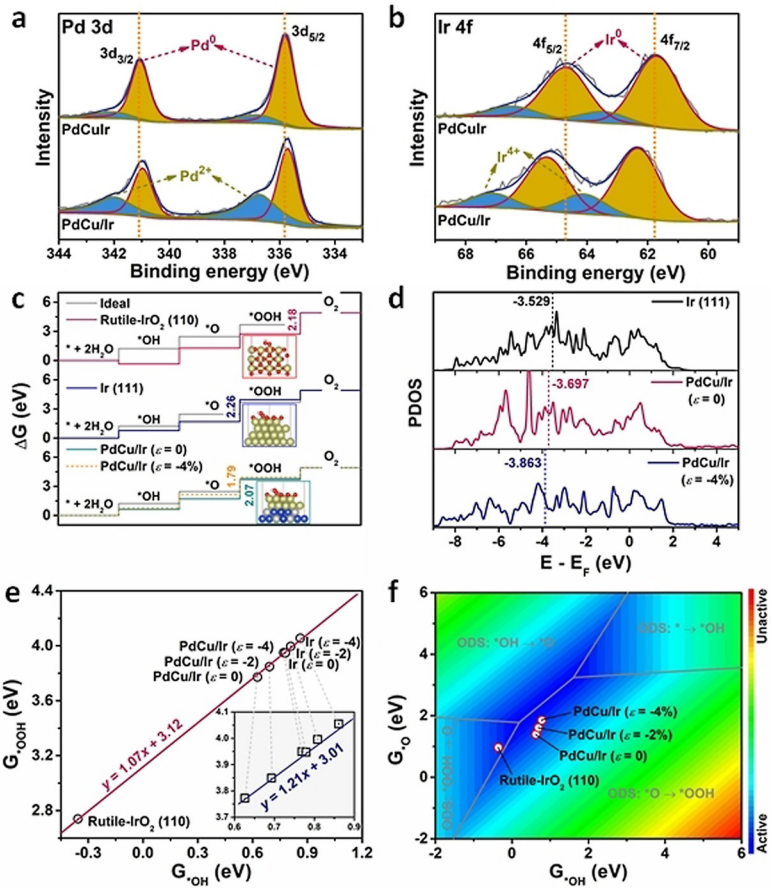

Figure 3. The mechanism for enhanced OER activity. XPS spectra and deconvoluted peaks of PdCu/Ir and PdCuIr nanocrystals in the regions of a) Pd 3d and b) Ir 4f. c) The OER free energy diagram for the ideal OER catalyst, rutile IrO2 (110) surface, Ir (111) surface, PdCu/Ir surface and strained PdCu/Ir surface at a zero applied potential (insets are the corresponding adsorption structures of *OOH. The Ir dark yellow, Cu blue, Pd gray, O red, H white). d) The calculated d-band density of states (DOS) of the surface atom on Ir (111), PdCu/Ir and PdCu/Ir under 4% compression (the vertical dashed lines indicate the d-band centers). e) The free energy of *OH as a function of the free energy of *OOH on IrO_2 (110), strained Ir (111), and PdCu/Ir surfaces (inset shows the free energy of *OH as a function of the free energy of *OOH on strained Ir (111) and PdCu/Ir surfaces). f) OER overpotential contour map in terms of the free energies of *OH and *O intermediates.

the PdCu/Ir core/shell nanocrystals. The following four-step reaction mechanism was considered to determine the free energy diagram for OER:[42]

$$H_2O + * \rightarrow *OH + H^+ + e^- \quad (1)$$

$$*OH \rightarrow *O + H^+ + e^- \quad (2)$$

$$*O + H_2O \rightarrow *OOH + H^+ + e^- \quad (3)$$

$$*OOH \rightarrow * + O_2 + H^+ + e^- \quad (4)$$

The free energy change in each reaction step was calculated based on the computational hydrogen electrode (CHE) model.[42,47] In the CHE model, the free energy of an electron-proton pair is estimated as half of the free energy of a H_2 molecule at standard conditions, which is then shifted by -eU upon an applied external potential U. Since the reaction cannot proceed unless all the reaction steps are exothermic, an ideal OER catalyst is such that the free energy change in each step equals 1.23 eV.[42] However, in practice, OER catalysts can have overpotentials greater than 1.23 V. More details about the OER free energy diagram calculation can be found elsewhere.[42]

To simulate the alloying effect in PdCu core on OER activity, we constructed a four-atomic-layer core/shell model based on *fcc* Ir (111) surface and replaced the bottom two layers with PdCu alloy. Oxygen covered (111) surfaces as opposed to the clean surfaces are considered in our calculations because OER is often inefficient on the latter due to their high oxygen-affinity.[48] Figure 3c shows the OER free energy diagrams on rutile-IrO_2 (110), Ir (111) and PdCu/Ir (111) surfaces at a zero applied potential ($U = 0$ V). The PdCu/Ir surface shows lowered reaction overpotential (2.07 V) compared with IrO_2 (110) (2.18 V) and Ir (111) surfaces (2.26 V), suggesting that the alloying is beneficial to OER activity. The overpotential-determining-step (ODS) is identified as step 4 ($*OOH \rightarrow * + O_2 + H^+ + e^-$) on IrO_2 (110) but step 3 ($*O + H_2O \rightarrow *OOH + H^+ + e^-$) on Ir (111) and PdCu/Ir surfaces. To examine the strain effect from lattice mismatch between PdCu core and Ir shell, we apply compressive strains to PdCu/Ir surface. Upon a compression of 4%, the OER overpotential is further reduced by 0.28 eV compared to the strain-free surface, explaining the improved OER activity on PdCu/Ir nanocrystals. These results establish that the alloying and straining are both responsible for the improved OER activity on PdCu/Ir core/shell nanocrystals.

Figure 3d displays the shift of the d-band centers for the atoms on Ir (111), PdCu/Ir and strained PdCu/Ir surfaces. Compared to the d-band center of Ir (111) surface (−3.529 eV), there is −0.17 eV shift of the d-band center on PdCu/Ir surface (−3.697 eV). The downshift of the d-band center is known to weaken the binding of the intermediates and to enhance OER activity. Under 4% compression, the d-band center of PdCu/Ir surface further downshifts to −3.863 eV, rendering the optimized OER activity of the strained PdCu/Ir structures among the three.

Linear scaling relation between the binding energies of *OH and *OOH intermediates on oxides has been reported for OER, with a slope close to 1 and an intercept of 3.2.[42] We identify a similar scaling relation ($G_{*OOH} = 1.07\,G_{*OH} + 3.12$) on IrO_2 (110), strained Ir (111) and PdCu/Ir surfaces (Figure 3e). Such scaling relation enables us to express the OER overpotential as a function of the free energies of only two independent intermediates, i.e., G_{*OH} and G_{*O}, on a contour plot (Figure 3f). Here, we divide the contour plot into four subregions according to the ODS. More specifically, the ODS for OER in the lower right subregion is step 3 ($*O + H_2O \rightarrow *OOH + H^+ + e^-$), while in the lower left is step 4 ($*OOH \rightarrow * + O_2 + H^+ + e^-$). The boundary between adjacent subregions (gray lines) thus defines an overpotential "trough" and the most active OER catalyst should reside at the bottom of the "trough". Placing the studied catalysts on the contour map, we find that strained PdCu/Ir sits very closely to the minimal overpotential "trough"; this suggests that PdCu/Ir nanocrystals are on a par with the most active catalysts for OER, including metals and rutile oxides, which is consistent with the experimental observations. It is worth noting that the minimal overpotential determined in Figure 3e (1.6 V) is 0.37 V higher than the overpotential on the ideal OER catalyst (1.23 V), which can be attributed to the scaling relation between G_{*OOH} and G_{*OH} ($G_{*OOH} = 1.07\,G_{*OH} + 3.12$). The difference between G_{*OH} and G_{*OOH} on the ideal OER catalyst is 2.46 eV, i.e., the sum of step 2 and step 3, which is excluded from the linear scaling relation. Nevertheless, we find that the scaling relation between G_{*OOH} and G_{*OH} can be optimized on the metal core–shell nanocrystals. For example, the minimal overpotential on the contour plot can be lowered to 1.55 V based on the linear scaling relation ($G_{*OOH} = 1.21G_{*OH} + 3.01$) determined solely from the strained Ir and PdCu/Ir (*inset* of Figure 3e). Therefore, there is still much room to further lower the overpotential on core/shell nanocrystals as superior OER electrocatalysts.

We then turned our attention to building a bridge between the strained core/shell structure and HER performance, and found that the strained PdCu/Ir/C also delivers excellent HER performance. We first tested the HER polarization curves of PdCu/Ir/C, PdCuIr/C and PdCu/C in N_2-saturated 0.1 M $HClO_4$ solution with a scan rate of 5 mV s^{-1}, and the commercial Pt/C and Ir/C were served as benchmark catalysts for comparing the electrocatalytic HER properties (Figure 4a). Among these electrocatalysts, the PdCu/Ir/C shows the lowest onset potential near 0 V (vs. RHE), very similar to that of the commercial Pt/C. The onset potential follows the order of PdCu/Ir/C ≈ Pt/C < PdCuIr/C < Ir/C < PdCu/C. Additionally, the overpotentials at a current density of 10 mA cm^{-2} of both PdCu/Ir/C and commercial Pt/C are only 20 mV, outperforming those of PdCuIr/C (27 mV), PdCu/C (45 mV) and Ir/C (33 mV) (Figure 4b). The HER current densities of the catalysts are further converted into noble metal mass-based activities to eliminate the different contributions derived from varied composition or structure to the HER activities. The mass activity of PdCu/Ir at −0.02 V (vs. RHE) is 1.23 A mg_{Pd+Ir}^{-1}, higher than those of PdCu/C (0.87 A mg_{Pd}^{-1}), PdCuIr/C (0.62 A mg_{Pd+Ir}^{-1}), Ir/C (0.48 A mg_{Ir}^{-1}) and Pt/C (0.96 A mg_{Pt}^{-1}) (Figure 4c), representing the enhanced HER activity of strained PdCu/Ir/C catalysts.

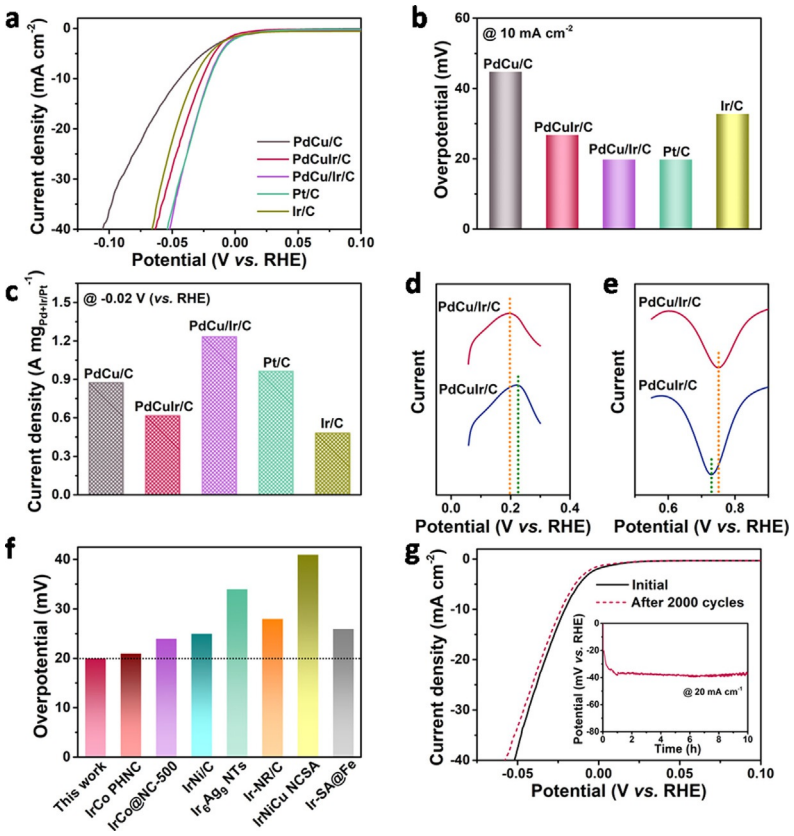

Figure 4. The electrocatalytic HER performance of different electrocatalysts in 0.1 M $HClO_4$. a) The HER polarization curves, b) the overpotential at a current density of 10 mA cm^{-2}, and c) current density normalized by the noble metal mass at −0.02 V (vs. RHE) of different electrocatalysts. The magnified d) hydrogen desorption peaks and e) the reduction potential curves in the CV curves of PdCu/Ir/C and PdCuIr/C. f) The HER overpotential at 10 mA cm^{-2} of the PdCu/Ir/C electrocatalyst and those of other representative Ir-based OER electrocatalysts reported recently in acidic media.[37,49–54] g) HER polarization curves before and after 2000 cycles (inset is CP measurement at a current density of 20 mA cm^{-2}) of PdCu/Ir/C.

Such enhanced HER activity can be supported by the strain tuning in achieving the appropriate binding strength of adsorbed intermediates (H*).[21] The compressive strain in our catalytic system can induce the downshift of d-band center relative to the Fermi level to maintain the inherent d occupancy.[24] As the d-band center is shifted down, the antibonding d states downshift meanwhile, thus leading to a weakened adsorption interaction for reaction intermediates, facilitating the enhanced HER activity. The CV measurements results of PdCu/Ir and PdCuIr nanocrystals in 0.1 M $HClO_4$ electrolyte are also tested to demonstrate the altered electronic structure, as well as visualize the strain effect (Figure S10). The potential of H adsorption/desorption peaks of PdCu/Ir is lower than that of PdCuIr, implying the weakened hydrogen binding energy (Figure 4d).[37] The positively shift of the reduction potentials of PdCu/Ir also indicate the weakened binding strength of the oxygenated species (Figure 4e).[28,45] In terms of the utilization of Ir atoms, Ir-based mass activity of PdCu/Ir/C is still far higher than the alloyed PdCuIr/C catalyst and other catalysts (Figure S11). Compared with the other state-of-the-art Ir-based electrocatalysts toward HER, the PdCu/Ir/C also shows lower overpotential and higher mass activity (Figure 4f & Table S2).[37,49–54]

The HER stability of the most active PdCu/Ir/C was further recorded by ADTs and CP technologies. As shown in Figure 4d, PdCu/Ir/C shows a negative shift of only 3 mV at 10 mA cm^{-2} after 2000 consecutive cycles with a scan rate of 50 mV s^{-1}. Furthermore, the CP curve is stable after 15 h durability test at a constant current density of 20 mA cm^{-2}, except for the slight fluctuation caused by a large number of bubbles at the later stage of the CP test (the *inset* of Figure 4d). After the long-term HER tests, the PdCu/Ir can well keep the structure, and very little Cu is lost in such harsh acidic conditions (Figure S12).

The excellent bifunctional electrocatalytic activities and stability of PdCu/Ir/C toward OER and HER promote us to design a water electrolyzer. The PdCu/Ir/C were deposited on the carbon paper to test for both cathode and anode (PdCu/Ir/C//PdCu/Ir/C) in 0.5 M H_2SO_4 electrolyte. Figure 5a shows the HER and OER polarization curves of PdCu/Ir/C on carbon paper in N_2 and O_2-saturated 0.5 M H_2SO_4 electrolyte without *IR*-correction. The overpotentials of HER and OER are only 21 mV and 344 mV at a current density of 10 mA cm^{-2}, respectively, and 46 mV and 380 mV at 20 mA cm^{-2}, respectively, indicating that the excellent bifunctional electrocatalytic activity can be well maintained at the high-concentration acidic environment. After assembling

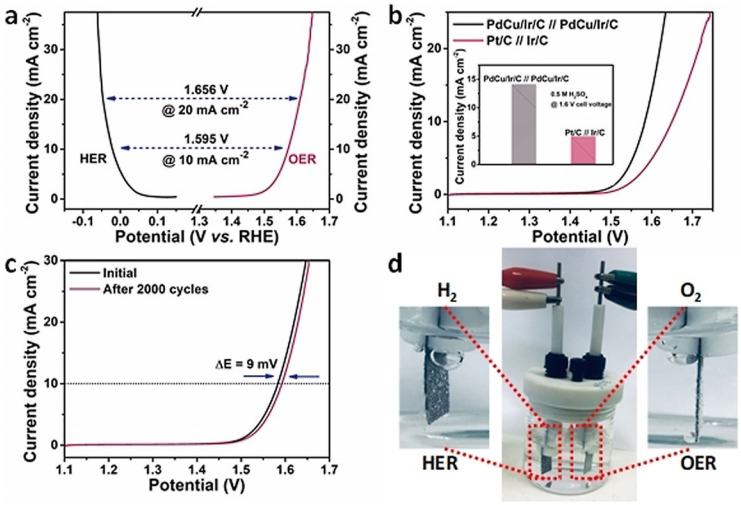

Figure 5. The electrocatalytic overall water splitting performance of PdCu/Ir/C in 0.5 M H_2SO_4. a) HER and OER polarization curves of PdCu/Ir/C. b) Polarization curves of PdCu/Ir/C // PdCu/Ir/C and Pt/C // Ir/C for overall water splitting. c) Polarization curves of PdCu/Ir/C // PdCu/Ir/C before and after 2000 cycles. d) The practical water electrolyzer in a working condition.

a two-electrode PdCu/Ir/C//PdCu/Ir/C system, an overpotential of 1.583 V can be achieved at a current density of 10 mA cm^{-2}, 67 mV lower than that of Pt/C//Ir/C system (Figure 5b). At 1.60 V cell voltage, the PdCu/Ir/C//PdCu/Ir/C electrolyzer can deliver a current density of 14.1 mA cm^{-2}, further revealing the high activity toward electrocatalytic overall water splitting (the *inset* of Figure 5b). After the consecutive 2000 cycles ADTs tests, the overpotential only decreases 9 mV, confirming the outstanding stability toward long-term service (Figure 5c). During the stability tests process, the continuous H_2 and O_2 bubbles can be rapidly generated on the both cathode and anode (Figure 5d).

Conclusion

In summary, well-characterized core/shell PdCu/Ir and trimetallic PdCuIr alloy nanocrystals were developed as the platform to illustrate the role of compressive surface strains in boosting acidic OER activities. The Ir shell with ≈4 ML is heteroepitaxially grown on a PdCu core to yield a compressive surface strain of 3.60% on the core/shell nanocatalysts. The ligand effect is eliminated on the relatively thick Ir shell. The exclusive strained PdCu/Ir nanocrystals achieve a low OER overpotential of 283 mV at a current density of 10 mA cm^{-2} and a high mass activity of 1.83 A mg_{Ir}^{-1} at 1.51 V (vs. RHE). DFT calculations reveal that the compressive strain on the Ir shell lowers the adsorption strength of oxygen containing intermediates, and downshifts the d-band center, thus facilitating the generation of oxygen molecules. These exclusive strained PdCu/Ir catalysts can also deliver high HER activities, and thus can realize a highly active overall water splitting electrolyzer with a low cell voltage of 1.583 V, while exhibiting excellent stability. Isolating the strain effect allows us to gain better understanding on strain engineering in electrochemical catalysis on metals-based core/shell nanostructures.

Acknowledgements

This study was financially supported by the National Science Fund for Distinguished Young Scholars (No. 52025133), Tencent Foundation through the XPLORER PRIZE, the Beijing Natural Science Foundation (JQ18005), National Key R&D Program of China (No. 2017YFA0206701), the Fund of the State Key Laboratory of Solidification Processing in NWPU (SKLSP202004), BIC-ESAT funding and the China Postdoctoral Science Foundation (No. 2019TQ0001 and 2020M670020). The work at California State University Northridge was supported by NSF-PREM program (DMR-1828019). The work at Institute of Physics, Chinese Academy of Sciences was supported by the National Natural Science Foundation of China (No. 52025025 and 52072400).

Conflict of interest

The authors declare no conflict of interest.

Keywords: core/shell structure · overall water splitting · oxygen evolution reaction (OER) · nanocrystals · strain effect

[1] W. Winsche, K. C. Hoffman, F. Salzano, *Science* **1973**, *180*, 1325–1332.
[2] M. Li, Z. Xia, Y. Huang, L. Tao, K. Yin, Y. Chao, W. Yang, W. Yang, Y. Yu, S. Guo, *Acta Phys. Chim. Sin.* **2020**, *36*, 1912049.
[3] Y. Jiao, Y. Zheng, M. Jaroniec, S. Z. Qiao, *Chem. Soc. Rev.* **2015**, *44*, 2060–2086.
[4] I. Roger, M. A. Shipman, M. D. Symes, *Nat. Rev. Chem.* **2017**, *1*, 0003.
[5] G. Glenk, S. Reichelstein, *Nat. Energy* **2019**, *4*, 216–222.
[6] C. Wang, L. Qi, *Angew. Chem. Int. Ed.* **2020**, *59*, 17219–17224; *Angew. Chem.* **2020**, *132*, 17372–17377.
[7] T. Zheng, C. Shang, Z. He, X. Wang, C. Cao, H. Li, R. Si, B. Pan, S. Zhou, J. Zeng, *Angew. Chem. Int. Ed.* **2019**, *58*, 14764–14769; *Angew. Chem.* **2019**, *131*, 14906–14911.

[8] J. Song, C. Wei, Z. F. Huang, C. Liu, L. Zeng, X. Wang, X. J. Xu, *Chem. Soc. Rev.* **2020**, *49*, 2196 – 2214.
[9] X. Li, L. Xiao, L. Zhou, Q. Xu, J. Weng, J. Xu, B. Liu, *Angew. Chem. Int. Ed.* **2020**, *59*, 21106 – 21113; *Angew. Chem.* **2020**, *132*, 21292 – 21299.
[10] J. Mahmood, F. Li, S. M. Jung, M. S. Okyay, I. Ahmad, S. J. Kim, N. Park, H. Y. Jeong, J. B. Baek, *Nat. Nanotechnol.* **2017**, *12*, 441 – 446.
[11] F. Luo, Q. Zhang, X. Yu, S. Xiao, Y. Ling, H. Hu, L. Guo, Z. Yang, L. Huang, W. Cai, H. Cheng, *Angew. Chem. Int. Ed.* **2018**, *57*, 14862 – 14867; *Angew. Chem.* **2018**, *130*, 15078 – 15083.
[12] H. N. Nong, L. J. Falling, A. Bergmann, M. Klingenhof, H. P. Tran, C. Spöri, R. Mom, J. Timoshenko, G. Zichittella, A. Knop-Gericke, S. Piccinin, J. Pérez-Ramírez, B. R. Cuenya, R. Schlögl, P. Strasser, D. Teschner, T. E. Jones, *Nature* **2020**, *587*, 408 – 413.
[13] Y. Li, Y. Sun, Y. Qin, W. Zhang, L. Wang, M. Luo, H. Yang, S. Guo, *Adv. Energy Mater.* **2020**, *10*, 1903120.
[14] L. C. Seitz, C. F. Dickens, K. Nishio, Y. Hikita, J. Montoya, A. Doyle, C. Kirk, A. Vojvodic, H. Y. Hwang, J. K. Norskov, T. F. Jaramillo, *Science* **2016**, *353*, 1011 – 1014.
[15] Q. Yao, B. Huang, N. Zhang, M. Sun, Q. Shao, X. Huang, *Angew. Chem. Int. Ed.* **2019**, *58*, 13983 – 13988; *Angew. Chem.* **2019**, *131*, 14121 – 14126.
[16] H. Chen, L. Shi, X. Liang, L. Wang, T. Asefa, X. Zou, *Angew. Chem. Int. Ed.* **2020**, *59*, 19654 – 19658; *Angew. Chem.* **2020**, *132*, 19822 – 19826.
[17] P. Lettenmeier, L. Wang, U. Golla-Schindler, P. Gazdzicki, N. A. Canas, M. Handl, R. Hiesgen, S. S. Hosseiny, A. S. Gago, K. A. Friedrich, *Angew. Chem. Int. Ed.* **2016**, *55*, 742 – 746; *Angew. Chem.* **2016**, *128*, 752 – 756.
[18] Y. T. Kim, P. P. Lopes, S. A. Park, A. Y. Lee, J. Lim, H. Lee, S. Back, Y. Jung, N. Danilovic, V. Stamenkovic, J. Erlebacher, J. Snyder, N. M. Markovic, *Nat. Commun.* **2007**, *8*, 1449.
[19] H. N. Nong, T. Reier, H. S. Oh, M. Gliech, P. Paciok, T. H. Thi Vu, D. Teschner, M. Heggen, V. Petkov, R. Schlögl, T. Jones, P. Strasser, *Nat. Catal.* **2018**, *1*, 841 – 851.
[20] J. Zhu, Z. Chen, M. Xie, Z. Lyu, M. Chi, M. Mavrikakis, W. Jin, Y. Xia, *Angew. Chem. Int. Ed.* **2019**, *58*, 7244 – 7288; *Angew. Chem.* **2019**, *131*, 7322 – 7326.
[21] Z. Xia, S. Guo, *Chem. Soc. Rev.* **2019**, *48*, 3265 – 3278.
[22] R. P. Jansonius, P. A. Schauer, D. J. Dvorak, B. P. Macleod, D. K. Fork, C. P. Berlinguette, *Angew. Chem. Int. Ed.* **2020**, *59*, 12192 – 12198; *Angew. Chem.* **2020**, *132*, 12290 – 12296.
[23] F. Podjaski, D. Weber, S. Zhang, L. Diehl, R. Eger, V. Duppel, E. Alarcón-Lladó, G. Richter, F. Haase, A. F. Morral, C. Scheu, B. V. Lotsch, *Nat. Catal.* **2020**, *3*, 55 – 63.
[24] T. Adit Maark, A. A. Peterson, *J. Phys. Chem. C* **2014**, *118*, 4275 – 4281.
[25] M. Luo, S. Guo, *Nat. Rev. Mater.* **2017**, *2*, 17059.
[26] P. Strasser, S. Koh, T. Anniyev, J. Greeley, K. More, C. Yu, Z. Liu, S. Kaya, D. Nordlund, H. Ogasawara, M. F. Toney, A. Nilsson, *Nat. Chem.* **2010**, *2*, 454 – 460.
[27] J. Zhao, B. Chen, F. Wang, *Adv. Mater.* **2020**, *32*, 2004142.
[28] M. Luo, Z. Zhao, Y. Zhang, Y. Sun, Y. Xing, F. Lv, Y. Yang, X. Zhang, S. Hwang, Y. Qin, J. Y. Ma, F. Lin, D. Su, G. Lu, S. Guo, *Nature* **2019**, *574*, 81 – 85.
[29] H. N. Nong, H. S. Oh, T. Reier, E. Willinger, M. G. Willinger, V. Petkov, D. Teschner, P. Strasser, *Angew. Chem. Int. Ed.* **2015**, *54*, 2975 – 2979; *Angew. Chem.* **2015**, *127*, 3018 – 3022.
[30] H. S. Oh, H. N. Nong, T. Reier, A. Bergmann, M. Gliech, J. F. de Araújo, E. Willinger, R. Schlögl, D. Teschner, P. Strasser, *J. Am. Chem. Soc.* **2016**, *138*, 12552 – 12563.
[31] J. Park, Y. J. Sa, H. Baik, T. Kwon, S. H. Joo, K. Lee, *ACS Nano* **2017**, *11*, 5500 – 5509.
[32] T. Kwon, H. Hwang, Y. J. Sa, J. Park, H. Baik, S. H. Joo, K. Lee, *Adv. Funct. Mater.* **2017**, *27*, 1604688.
[33] S. Kumari, B. P. Ajayi, B. Kumar, J. B. Jasinski, M. K. Sunkara, J. M. Spurgeon, *Energy Environ. Sci.* **2017**, *10*, 2432 – 2440.
[34] H. Guo, Z. Fang, H. Li, D. Fernandez, G. Henkelman, S. M. Humphrey, G. Yu, *ACS Nano* **2019**, *13*, 13225 – 13234.
[35] J. Shan, C. Guo, Y. Zhu, S. Chen, L. Song, M. Jaroniec, Y. Zheng, S. Z. Qiao, *Chem* **2019**, *5*, 445 – 459.
[36] C. Shang, C. Cao, D. Yu, Y. Yan, Y. Lin, H. Li, T. Zheng, X. Yan, W. Yu, S. Zhou, J. Zeng, *Adv. Mater.* **2019**, *31*, 1805104.
[37] F. Lv, W. Zhang, W. Yang, J. Feng, K. Wang, J. Zhou, P. Zhou, S. Guo, *Small Methods* **2020**, *4*, 1900129.
[38] Z. Cheng, B. Huang, Y. Pi, L. Li, Q. Shao, X. Huang, *Natl. Sci. Rev.* **2020**, *7*, 1340 – 1348.
[39] T. Adit Maark, B. R. K. Nanda, *J. Phys. Chem. C* **2017**, *121*, 4496 – 4504.
[40] J. K. Nørskov, T. Bligaard, J. Rossmeisl, C. H. Christensen, *Nat. Chem.* **2009**, *1*, 37 – 46.
[41] Y. Zheng, Y. Jiao, A. Vasileff, S. Z. Qiao, *Angew. Chem. Int. Ed.* **2018**, *57*, 7568 – 7579; *Angew. Chem.* **2018**, *130*, 7690 – 7702.
[42] I. C. Man, H. Y. Su, F. Calle-Vallejo, H. A. Hansen, J. I. Martínez, N. G. Inoglu, J. Kitchin, T. F. Jaramillo, J. K. Nørskov, J. Rossmeisl, *ChemCatChem* **2011**, *3*, 1159 – 1165.
[43] K. Jiang, P. Wang, S. Guo, X. Zhang, X. Shen, G. Lu, D. Su, X. Huang, *Angew. Chem. Int. Ed.* **2016**, *55*, 9030 – 9035; *Angew. Chem.* **2016**, *128*, 9176 – 9181.
[44] S. Lu, Z. Zhuang, *J. Am. Chem. Soc.* **2017**, *139*, 5156 – 5163.
[45] M. Li, M. Luo, Z. Xia, Y. Yang, Y. Huang, D. Wu, Y. Sun, C. Li, Y. Chao, W. Yang, W. Yang, Y. Yu, S. Guo, *J. Mater. Chem. A* **2019**, *7*, 20151 – 20157.
[46] T. Tang, W. J. Jiang, S. Niu, N. Liu, H. Luo, Y. Y. Chen, S. F. Jin, F. Gao, L. J. Wan, J. S. Hu, *J. Am. Chem. Soc.* **2017**, *139*, 8320 – 8328.
[47] J. K. Nørskov, J. Rossmeisl, A. Logadottir, L. Lindqvist, J. R. Kitchin, T. Bligaard, H. Jónsson, *J. Phys. Chem. B* **2004**, *108*, 17886 – 17892.
[48] A. Wang, Z. Zhao, D. Hu, J. Niu, M. Zhang, K. Yan, G. Lu, *Nanoscale* **2019**, *11*, 426 – 430.
[49] J. Feng, F. Lv, W. Zhang, P. Li, K. Wang, C. Yang, B. Wang, Y. Yang, J. Zhou, F. Lin, G. C. Wang, S. Guo, *Adv. Mater.* **2017**, *29*, 1703798.
[50] P. Jiang, J. Chen, C. Wang, K. Yang, S. Gong, S. Liu, Z. Lin, M. Li, G. Xia, Y. Yang, J. Su, Q. Chen, *Adv. Mater.* **2018**, *30*, 1705324.
[51] M. Zhu, Q. Shao, Y. Qian, X. Huang, *Nano Energy* **2019**, *78*, 330 – 337.
[52] F. Luo, L. Guo, Y. Xie, J. Xu, K. Qu, Z. Yang, *Appl. Catal. B* **2020**, *279*, 119394.
[53] J. Zhang, Z. Chenm, C. Liu, J. Zhao, S. Liu, D. Rao, A. Nie, Y. Chen, Y. Deng, W. Hu, *Sci. China Mater.* **2020**, *63*, 249 – 257.
[54] F. Luo, H. Hu, X. Zhao, Z. Yang, Q. Zhang, J. Xu, T. Kaneko, Y. Yoshida, C. Zhu, W. Cai, *Nano Lett.* **2020**, *20*, 2120 – 2128.

Manuscript received: December 5, 2020
Accepted manuscript online: January 12, 2021
Version of record online: March 3, 2021

